Design of a compact, high-resolution velocity-map imaging spectrometer for attosecond spectroscopy

D. Platzer, A. Autuori, C. Schouder, M. Lejman, L. Maëder, H J B Marroux, C. Pothier, P. Salières, L. Poisson

Design of a Compact, High-resolution Velocity-Map Imaging Spectrometer for Attosecond Spectroscopy

D. Platzer,[1] A. Autuori,[1] C. Schouder,[2,1,a)] M. Lejman,[1] L. Maeder,[1] H.J.B. Marroux,[1] C. Pothier,[1] P. Salières,[1,b)] and L. Poisson[2]
[1)] *Université Paris-Saclay, CEA, LIDYL, 91191 Gif sur Yvette, France*
[2)] *Université Paris-Saclay, CNRS, Institut des Sciences Moléculaires d'Orsay, 91405 Orsay, France*

(Dated: 12 November 2024)

We present the design of a VMI spectrometer optimized for attosecond spectroscopy in the 0-40 eV energy range. It is based on a compact 3-electrode configuration where the lens shape, size and material have been optimized using numerical simulations to improve the spectral resolution by a factor ∼5 relative to the initial design[1] while keeping a flat spectral response in the 10-40 eV range. The experimental performance is tested using an attosecond source based on high-order harmonic generation. A good agreement is observed between the measured and simulated spectral resolution. At low kinetic energy, the electrostatic lens remains the limiting factor, while the high energy range is mostly affected by the resolution of the camera objective.

I. INTRODUCTION

During the last decades, the development of attosecond light pulses in the extreme ultraviolet (XUV) range using the process of high-order harmonic generation (HHG), and more recently using X-ray free electron lasers, has allowed the investigation of ultrafast dynamics in matter on the attosecond timescale. Of particular significance are the measurements of photoemission time delays, related to the so-called Eisenbud-Wigner-Smith scattering delays[2–4], in a large variety of systems, from atoms[5,6], molecules[7,8] and nanoparticles[9] to liquids[10] and solids[11]. These studies were made possible by combining attosecond spectroscopic techniques, based on the reconstruction of attosecond beating by interference of two-photon transitions (RABBIT)[12] and attosecond streaking[13,14] methods, with advanced detection schemes for the emitted electrons. Concerning the latter, the large spectral bandwidth (10's of eV) of the XUV pulses requires spectrometers with a large detection range. Furthermore, the presence of structured continua around, e.g., autoionizing or shape resonances calls for high resolution in order to access the full ionization dynamics in these spectral regions[15–19]. The required spectral range and resolution were initially obtained using time-of-flight electron spectrometers, in particular magnetic bottle electron spectrometers (MBES), thereby solely accessing the energy of the emitted particle, while only few studies focused on the photoemission direction[20,21]. However, a strong interest recently developed onto moving to angularly-resolved measurements. Extensive work performed both theoretically[22–24] and experimentally[25–28] showed that the attosecond dynamics under study may present strong variations with the electron emission angle in rare gases[29,30] or in molecules[31,32]. Besides, the angular resolution could provide new detection schemes[33–36] accessing to new types of information.

Spectrometers measuring photoelectron angular distributions (PAD) can be grouped in two families. First, the COLd Target Recoil Ion Momentum Spectrometers (COLTRIMS)[37,38] access the complete 3D momentum vectors of ionic fragments and electrons. To that end, the electrons and ions are guided towards time and position-sensitive detectors by using a combination of electric and magnetic fields. By recording them in coincidence and using vector correlations, so-called complete experiments can be performed for rapid dissociation channels[39,40].

Second, the Velocity-Map Imaging Spectrometers (VMIS) measure a 2D projection of the electron or ion momentum distribution through the use of an electrostatic lens combined with a position-sensitive detector. The detector can be backed by either a delay-line anode or a phosphor screen. With a delay-line anode, the 3D momentum can be retrieved as in COLTRIMS, the number of events is then limited to a few per laser shot. The phosphor screen is the most standard approach and is used in combination with a camera to capture the light flashes. According to the repetition rate of the ionizing source and the shutter time of the camera, coincidence/covariance measurements can also be achieved[41,42]. There are several approaches to retrieve the 3D momentum in the case of a VMIS backed with a phosphor screen[43]. First, this can be achieved in the measurement itself, e.g., using slice-imaging[44], or by tomographic imaging[45]. In fact, for fast phosphor screens (dead time < 100 ns), the development of new sensors[46,47] now permits to retrieve the time information that is usually lacking with standard cameras. The time resolution for these sensors is now sufficient to access the 3D momentum of ions but is still too poor for photoelectrons compared to delay-line detectors. The major challenge comes from the difficulty to precisely assess the velocity component of the photoelectron along the detector axis. The main approach to solve this issue is to change the spectrometer length to stretch the photoelectron signal sufficiently to be resolved with time-to-digital converter. This development has been pioneered by Li[48] and has now been applied successfully onto multiple experimental setups[43,49–51].

Second, the most standard method to access the 3D mo-

a)constant.schouder@universite-paris-saclay.fr
b)pascal.salieres@cea.fr

mentum is to use Abel inversion methods[52–55]. This approach imposes specific geometrical constraint between the polarization of the light and the axis of the detector as it relies on a cylindrical symmetry in the probing process. We also note the development of novel arrangements which permits to obtain images directly in the polarization plane of the laser pulse[56,57]. Concerning standard VMIS configurations, various strategies were used to further improve the imaging resolution of the initial design proposed by Eppink and Parker [1]: addition of deflectors[58], increasing number of electrodes[59,60], double lens configuration[61,62] or electrode shape optimization[63,64], which can sometimes be at the expense of compacity and simplicity of operation.

Here we present a recently developed VMIS designed for attosecond photoelectron spectroscopy in the 0-40 eV spectral range. The VMIS design was elaborated to retain a compacity and simplicity of use with only 3 electrodes while maintaining a high resolution over a large spectral range. This article is structured as follows: First, we present the SIMION simulations that determine the spectrometer layout and its expected resolution. Second, we introduce the compact design of the VMIS with its different components. Third, we compare the predicted spectral resolution with experimental measurements performed using an attosecond pulse train previously characterized in a magnetic bottle electron spectrometer.

II. SIMULATIONS

As introduced, the design is based on an electrostatic lens composed of three electrodes: repeller, extractor and ground such that for a fixed repeller voltage, only the extractor voltage has to be tuned to optimize the electron beam focusing. To improve the performance of the lens, the shapes and sizes of the electrodes have been optimized using numerical simulations of electron trajectories with the SIMION software[65]. The idea of changing the geometry of the electrodes is inspired by previous work[63,64] on ion imaging. It consists here in giving a cylindrical shape to the repeller and a conical shape to the extractor and to the ground electrode.

The influence of the different geometric parameters of the electrostatic lens has been studied by varying each parameter to minimize the spread of zero-kinetic energy electrons. This was done "by hand" to identify which parameters were most critical in determining the overall behavior of the lens. It was found that the extractor profile was particularly important, especially its minimum diameter and its conical shape (modeled initially as a triangular section then later modified to a thinned conical shape to ease the fabrication in mu-metal, see below). To a lesser extent, the profile of the repeller as well as the extractor/ground distance had a notable influence on the quality of the focus. Finally, the conical shape of the ground had a weak impact on the final results.

The final design of the electrostatic lens is presented in Figure 1 as a SIMON view. It shows a cut through the cylindrically-symmetric lens annotated with the relevant distances between the different composing elements. With a flight length of 250 mm, a detector of 75 mm diameter and

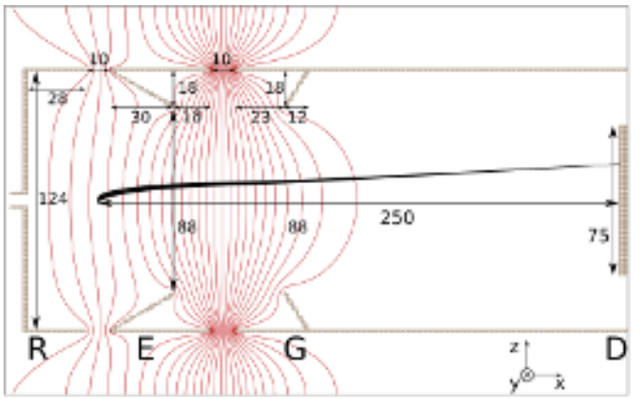

FIG. 1. SIMION view of the electrostatic lens, with equipotential lines plotted in red. R, E, G, D stand for Repeller, Extractor, Ground and Detector, respectively. All numbers are given in mm. The distance between the interaction region and the detector is 250 mm. As an illustration, 21 electrons with a fixed kinetic energy of 20 eV along z were flown with a starting z position ranging from -1.5 mm to 1.5 mm. Their trajectories are shown in black lines for V_{Rep} = -5 kV and V_{Extr} = -4 kV.

a repeller voltage of -5 kV, the maximum electron energy that can be detected is estimated to be 44 eV. Note that the electrostatic optics assembly may handle a repeller voltage of at least -10 kV without arcing, giving the ability to detect electrons up to ∼88 eV (cf. next section for details).

Regarding the spectral resolution, a key element is the size of the ionization region in a typical experiment. Actually, simulations show that it is not the absolute size but rather the size relative to the lens dimension that matters. A first strategy is then to reduce the size of the interaction region for a given lens size. Generally, it corresponds to the intersection of the focused light beam with the atomic/molecular beam and has a cylindrical shape. In a typical experiment, the diameter of this cylinder is smaller than its length (typically, a few hundred microns diameter and a few millimeters long). In the simulations, we consider electrons starting over an extended spatial region consisting of a cylinder of ρ = 100 µm radius and l = 3 mm length along the y direction (laser propagation direction). Experimentally, the length of this cylinder, which is generally the largest dimension and consequently the resolution limiting factor, can be reduced by moving the gas jet away from the skimmer, and thus from the light beam, but this is at the expense of gas density. A second strategy consists in enlarging the lens size to make the interaction region appear comparatively smaller. For this reason, the whole lens dimension has been scaled up so that the inner diameters of the electrodes range between 88 mm and 124 mm, which is twice to four times larger than dimensions usually chosen[1,59,63]. To keep the external dimensions of the spectrometer while increasing the lens size, the idea has been to fabricate the electrodes directly in mu-metal to avoid the need of a shielding tube, see next Section.

To compare the performance of the electrostatic lens with the original design[1], we first simulate the trajectories of zero

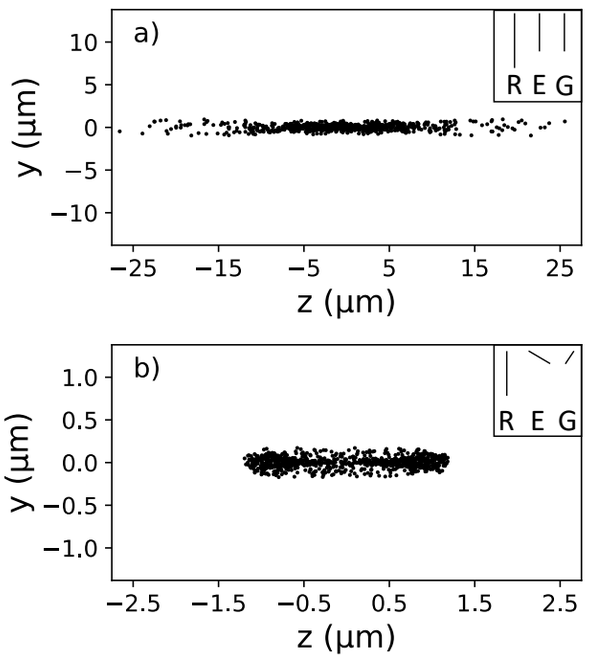

FIG. 2. Zero-energy electron distributions recorded in the detection plane with a cylindrical initial distribution in space (ρ = 100 μm, l = 3 mm) and V_{Rep} = -5 kV for a) a standard VMI configuration (V_{Extr} = -3.569 kV), b) the design presented here (V_{Extr} = -4.019 kV), sketched in each panel. Notice the factor of ten between the two scales.

kinetic energy electrons. Figure 2 shows the results of such simulations when comparing to a standard lens design with three flat electrodes spaced by 15 mm and with a diameter of 66 mm; the extractor and ground electrodes have an open area of 20 mm diameter. For these simulations, 900 electrons are flown with an initial position generated randomly within the ionization region. The electron positions recorded in the detection plane (yz plane) are plotted in Figure 2. For a repeller voltage fixed at -5 kV, the optimum extractor voltage has been found by minimizing the recorded spatial distribution extension. After this minimization process, the focal spot is around ten times smaller for our lens configuration than for the standard case.

In order to quantify the spectral resolution of the electrostatic lens over the energy range, we then run simulations consisting in flying bunches of 10^5 electrons in the following conditions: 1) All electrons start with the same non-zero initial energy; 2) Their initial emission direction is set randomly, but in the detection plane only (yz in Figure 1). This last condition creates a ring-shaped distribution on the detector that exempts us from Abel-inverting the recorded distributions. This technique, that could be called numerical slicing, was compared with the case of using a full isotropic initial distribution, the result of which was subsequently Abel-inverted. Since the recovered spatial widths of the electron peaks were comparable, the first method is used for all the simulations presented here. The energy resolution is then estimated by looking at the spatial spread of the resulting distribution on the detector. The electron positions on the detector are recorded and binned on a 4096×4096 grid. The thickness ΔR and radius R of the ring are then evaluated and converted to absolute and relative energy resolutions (ΔE and $\Delta E/E$ respectively) thanks to the relation:

$$\frac{\Delta E}{E} = 2\frac{\Delta R}{R} \tag{1}$$

which is the direct consequence of the $E \propto R^2$ relationship between radius and energy[1].

To estimate the energy resolution over the whole spectral range of the spectrometer, simulations are performed for initial electron energies varying from 1 to 44 eV by steps of ∼5 eV. For a fixed value of the repeller voltage, the extractor voltage can be tuned to get the best velocity focusing conditions at a specific energy. Thus, the simulations are performed for different extractor voltages corresponding to the optimum focusing at different electron energies. Figure 3(a) shows the predicted relative energy resolutions for a standard VMI, black curve, and for the new design, green curve, for an optimum focusing at 20 eV. The simulations foresee a better resolution for the latter for all energies, with up to a factor 5 improvement in the 20 eV region and values below 1% in the 10-40 eV range.

This improvement has two main origins. First, by doubling the lens dimensions, the resolution is improved by a factor of 2, all other parameters kept identical, as confirmed by simulations. Second, the original design for the electrode shapes accounts for the remaining improvement factor.

Figure 3(b) extends the range of interest for different extractor voltages, each voltage has been chosen to optimize the resolution for a specific electron kinetic energy displayed in the legend. Optimized energy resolution can reach values below 1% over a broad range, demonstrating the potential of this design. The question that one may ask is then whether such resolution can indeed be achieved in real conditions. It is important to note that the values displayed on Figure 3(b) depend on the size l of the interaction region. In the simulations, a close-to-linear relationship between l and the resolution is found, enabling a potential homothetic rescaling of the simulated values if the experimental value of l had to be different.

Putting aside the limitations introduced by the spatial extension of the interaction region that could in principle be taken into account in the simulations, the remaining limiting factor is probably the spatial resolution of the detector. Each element that composes it has to be considered: micro-channel plates (MCPs), phosphor screen, camera, and camera lens. Let us consider again the case of 20 eV electrons. The spatial resolution given by the simulations above is around 20 μm. However, the MCPs with a large surface, as the ones used in VMI systems, hardly reach this resolution and have then to be chosen carefully not to deteriorate the electrostatic lens resolution too much. An important parameter is then the number of amplification stages. For instance, given a channel size of 10 μm, the spatial resolution of a single stage of amplification lies between 50 and 100 μm while it reaches 150 μm for the double

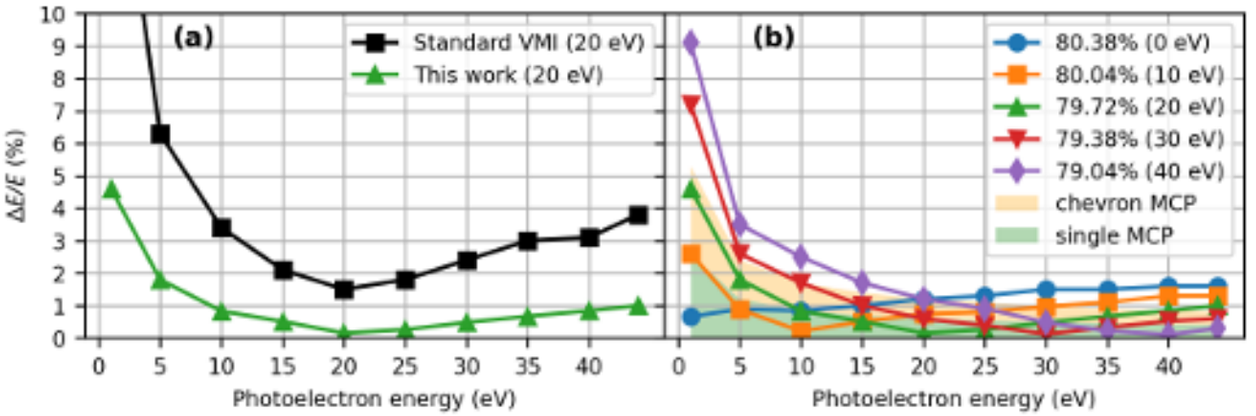

FIG. 3. Relative energy resolution for different designs of the VMIS and for different scaled focusing voltages with $V_{\mathrm{Rep}} = -5$ kV, obtained from SIMION simulations. The extractor voltages are chosen to optimize the velocity focusing conditions for a specific photoelectron kinetic energy shown in the legend. The other parameters are the same as in Figure 2. **(a)** Comparison between a standard VMIS lens (black square curve) and the one presented here (green triangle curve), the extractor voltages were -3.535 kV and -3.986 kV respectively. **(b)** Relative energy resolution of the spectrometer in Figure 1 for different scaled focusing voltages. The percentage values in legend refer to the ratio of potentials used, $V_{\mathrm{Extr}}/V_{\mathrm{Rep}}$. The orange and green surfaces correspond to the estimated resolution of chevron MCPs and single MCP respectively.

amplification stage in chevron MCPs[66]. Thus, in first approximation, there is a factor 2 between the spatial resolutions of chevron MCPs and single MCP. These two spatial resolutions are converted into energy resolution and plotted as orange and green surfaces on Figure 3(a) to determine where the MCP becomes the limiting factor. In the case of a chevron configuration, the resolution of the electrostatic lens is almost all the time located within the orange area, where the MCPs contribution is the limiting factor, whereas with a single configuration (green area), it is only limiting for photoelectron energies below 5 eV. This motivated our choice of a single MCP for the detection system, at the expense of signal amplification.

III. VMIS DESIGN

A picture of the electrostatic lens with the labeled relevant components is shown on Fig. 4. The electrodes are assembled using Polytetrafluoroethylene (PTFE) rings and maintained with eight Nylon rods, placed outside of the focusing region of the electrostatic lens, then allowing a complete cylindrical symmetry to its inner region. The ring between the repeller and extractor is drilled to let the laser beam enter and exit as well as to inject gas.

Gas injection is performed with a continuous jet mounted on a three-axis manipulator (Vinci Technologies MT3Z 100) to be aligned with a molecular beam skimmer (Beam Dynamics, Model 1, 0.5 mm or 1.0 mm orifice diameter). The ensemble can be installed at two locations to be able to inject gas along the electrostatic lens axis or perpendicular to it. The reason is as follows: when gas is injected perpendicular to the electrostatic lens direction, it is possible to measure the temperature of the supersonic jet by looking at the ion speed distribution. However, it forces the jet to be quite far from the interaction region, then imposing a low gas density at its location, meaning a potentially low level of signal. To be able to work at higher densities was added the possibility to inject gas directly through the repeller, thus reducing the distance to the interaction region.

The large dimension of the electrostatic lens presents space issues. In VMI systems, it is usually surrounded by a mu-metal sheet to shield from external magnetic fields -especially when detecting electrons- and the ensemble has to fit into a vacuum chamber. In order to shield the electrostatic lens in the most compact way, the idea was to manufacture the electrodes in mu-metal directly. This idea seemed reasonable as it was noted that the outer shape of the electrostatic lens was very similar to a cylinder, as can be seen on Figs.1 and 4. With the space saved, the electostatic lens could then fit into a customized NW250ISO-K six way cross. In the region beyond the ground electrode, a mu-metal cylinder (1.5 mm thick) is added to extend the shielding up to the detector. Its diameter is the same as the outer diameter of the electrodes and is modeled as a prolongation of the ground electrode as can be seen on Figure 1. It is additionally drilled with several holes to help for the pumping of the detection region.

The detector consists in a single micro-channel plate backed by a P43 phosphor screen mounted on a vacuum flange (Photonis APD 1 PS 75/12/10/8 I 60:1 NR). A sCMOS camera (PCO Edge 4.2 USB) is used to record the light emitted from the phosphor screen. To fully capture the detector area, a Xenon 0.95/25 (Schneider-Kreuznach) objective is mounted onto the camera. Additionally a green filter is placed in front of the objective to remove scattered infrared light. A $\sim$300 ns voltage gate is applied to the MCP to filter out secondary electrons that may hit the detector. The distance between the interaction region and the detector is 250 mm. The source and detector chamber are pumped with turbomolecular pumps (Ley-

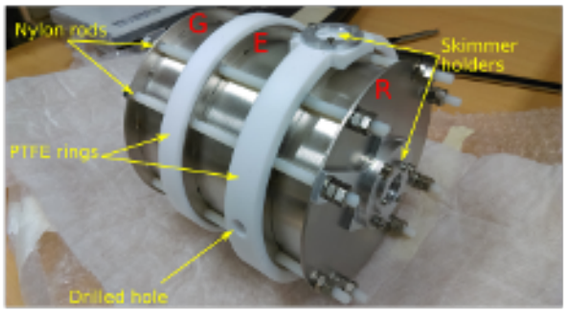

FIG. 4. Picture of the electrostatic lens assembly. R, E and G stand for Repeller, Extractor, Ground. See text for details.

bold Turbovac Mag W 2200iP and Pfeiffer ATH500M respectively).

IV. EXPERIMENTAL IMPLEMENTATION AND CALIBRATION

To measure the effective resolution of this new VMIS design over the 0-40 eV range, we have used the frequency comb obtained by high-harmonic generation, that corresponds in the time domain to a train of attosecond pulses[12]. The effective resolution is defined here as the peak broadening due to convolution with the spectrometer response (assumed Gaussian). In order to measure it, an XUV beamline in a two-foci configuration[68,69] is used, where the harmonic source is first characterized at the first focus and then used to calibrate the VMIS at the second focus. In the rest of the text, we will refer to the peak width as the standard deviation extracted from the Gaussian fit of the peak.

1. XUV source characterization

The high-order harmonics are generated by focusing a 25-fs 800-nm 4-mJ Titanium:Sapphire beam on a 2-cm cell filled with neon, reaching a $\sim 7\times10^{14}$ W/cm^2 intensity. The outgoing beam goes through a holey mirror that removes most of the fundamental beam while letting through the more collimated harmonic emission. The harmonic beam is then focused by a $f = 0.5$ m toroidal mirror in a $2f$-$2f$ configuration into a Magnetic Bottle Electron Spectrometer (MBES) in which neon is injected. This first electron spectrometer, which spectral resolution is approximated as $R_{\mathrm{MBES}} = 0.7 \pm 0.25\%$ over the 0-40 eV range (see Appendix B), is used to characterize the harmonic widths. The beam is then refocused by a second $f = 0.5$ m toroidal mirror into the VMIS and detected in neon. Assuming that the harmonic profiles and the spectral response of the MBES can be modeled by Gaussian functions, the effective harmonic width can be written as:

$$\Delta E_{H_N} = \sqrt{\Delta E^2_{\mathrm{MBES}} - (E_{H_N} \times R_{\mathrm{MBES}})^2} \qquad (2)$$

where ΔE_{MBES} and E_{H_N} are the measured photoelectron peak width and peak energy corresponding to harmonic N.

2. Detection in the VMIS

Electron images are obtained by photo-ionizing neon by the previously described harmonics. The repeller and extractor voltages are set to -4.889 and -3.885 kV, respectively. This choice is motivated by the accessible energy range (44 eV) and the voltage ratio (0.795) that is optimal for electrons in the 20-30 eV energy range according to Figure 3. Figure 5(a) shows the experimental 2D-photoelectron momentum image and its Abel inversion. In this case, the low kinetic energy electrons (image center around 0 a.u.) are not well focused as predicted by the simulations (green triangle in Figure 3(b)). A slight broadening of the distributions can be observed on the upper left of the image and is attributed to a residual magnetic field. Moreover a background signal is also present and is ascribed to the residual gas in the interaction chamber.

Figure 5(b) shows the angularly-integrated signal after Abel inversion of the raw 2D image with the DAVIS algorithm[70]. The images have been first circularized to correct for angular distortion in the detection (see Appendix D). The harmonic peaks corresponding to odd orders 15-33 are well resolved and can be identified easily up to 30 eV. From the position of each peak, we calculate the mapping between radius and energy. The results are discussed in Appendix A.

The Abel inversion procedure gives the different contributions in terms of Legendre polynomials from which we can extract the anisotropy parameters over each peak. The results are displayed in Figure 5(c). For energies below 25 eV, a relatively good agreement for β_2 is obtained with respect to synchrotron measurements[67]. For energies above 25 eV, there is an increasing mismatch. We rationalize this behavior by observing that the contribution of β_4 grows rapidly over this region. This may indicate that we are no longer in a single-photon absorption scheme. We believe that residual infrared light from the fundamental laser was still present in this measurement, possibly inducing two-photon XUV+IR transitions. Since the probability of the latter increases with photoelectron kinetic energy[71], this would lead to a distortion of the β_2 contribution and the appearance of a non-zero β_4 contribution at high energy. The decreasing contrast of the harmonic peaks with energy in the spectrum of Figure 5(b) may be the consequence of the appearance of so-called sidebands in between the main peaks due to XUV+IR transitions. Note that spatial distortions induced by the VMI electrostatic lens are another possible reason for the observed beahavior.

To quantify the spectrometer resolution in this regime, we evaluate the width of each harmonic peak, by fitting a Gaussian over each peak and extracting its standard deviation ΔE_{VMIS}. An equivalent of Equation 2 for the VMIS is then used to estimate the relative VMIS resolution $\Delta E_{\mathrm{VMIS}}/E$. It is plotted on Figure 6 and compared to:

- the resolution limit of the MCP (here single) determined as previously;
- the resolution limit of the camera, determined by measuring the average spreading of isolated electrons over the camera field (see Appendix E);

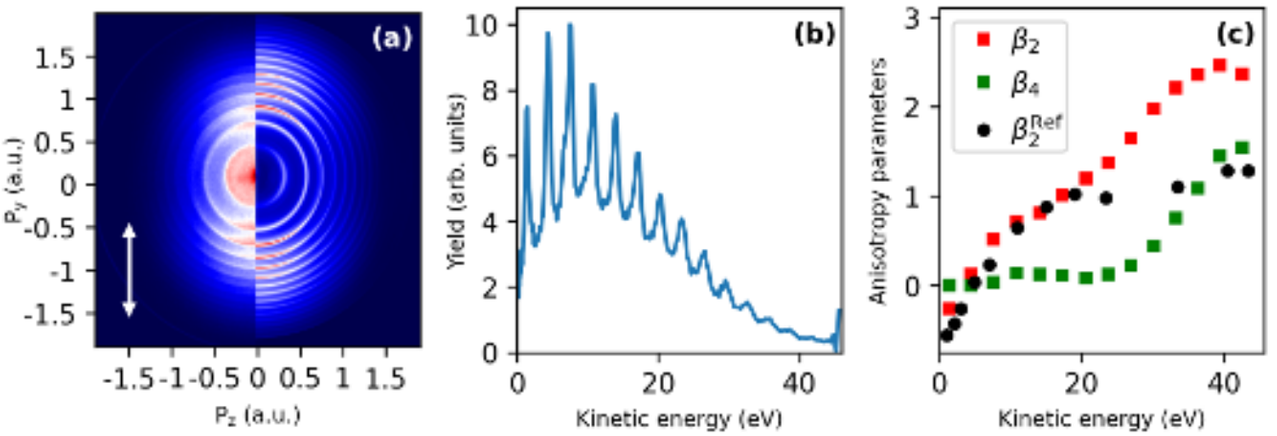

FIG. 5. (a) Raw 2D-momentum / Abel inverted 3D-momentum (left/right) distribution of photoelectrons ejected from Ne by a comb of high-order harmonics in the extreme ultraviolet. (b) Photoelectron kinetic-energy distribution obtained by angular integration of the complete 3D distribution. (c) Comparison of β_2 and β_4 parameters (red and green squares) extracted from the Abel inversion with β_2^{Ref} obtained from synchrotron measurements[67] (black circles).

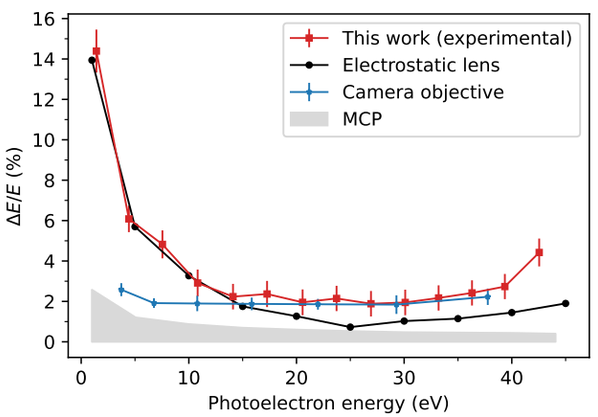

FIG. 6. Relative energy resolution measured for the VMIS (red square) as compared to the MCP resolution (grey area), the camera resolution (blue stars) and the electrostatic lens performance (black circles).

- the expected performance for the electrostatic lens determined by simulations with SIMION. These simulations differ from Figure 3 only by the length of the interaction zone that was tuned to be 7.5 mm instead of 3 mm. Experimentally, this long interaction length can be understood by a non-sufficiently efficient gas pumping leading to residual gas extending the ionization region. This was verified by imaging the photoelectrons in position imaging mode.

The measured VMIS resolution is around 2% over a wide range, from 15 to 35 eV. It degrades strongly at lower energies and less drastically at high energies. The comparison with the predictive curves shows that this resolution is limited by the electrostatic lens performance at energies below 15 eV and by the camera resolution above 15 eV (the latter is an improvement target for further studies).

Lastly, we compare these results with that obtained with the thick-lens design proposed by Kling et al.[59] in Figure 7. The latter is based on a spatial extension of the applied field using 11 electrodes that allows measurements up to 360 eV energies with -10 kV repeller voltage, while keeping a high resolving power over a wide range of energies. The experimental performance was tested using photoelectrons originating from laser-induced Above-Threshold-Ionization (ATI) or from XUV-induced ionization by a HHG source. In both cases, the intrinsic spectral widths of the photoelectron peaks were not measured and supposed not to be the limiting factor. The operation voltages were optimized to achieve a good resolution up to 60 eV (black circles) or up to 20 eV (blue circles). The comparison with the modified 3-electrode design (red squares) shows similar performances over the 0-40 eV range. As also stressed in Kling et al.[59], the resolution strongly depends on the effective interaction length that vary according to the performed experiment, and possibly within a given experiment according to the photoelectron energy.

V. CONCLUSION

A new VMI design was presented, implemented and characterized, aiming at attosecond spectroscopy over bandwidths of 10's of eV. It is based on a 3-electrode configuration as initially proposed by Eppink and Parker[1], but with cylindrical and conical shapes for the electrodes. The shapes and sizes of the latter have been optimized using SIMION simulations, and they were fabricated with mu-metal to shield from magnetic fields. This VMIS can image photoelectrons up to 44 eV using -5 kV repeller voltage and up to 88 eV -without any change on the design- using -10 kV. Simulations predict a resolution below 1% over a broad range (10-40 eV) for a 3-mm

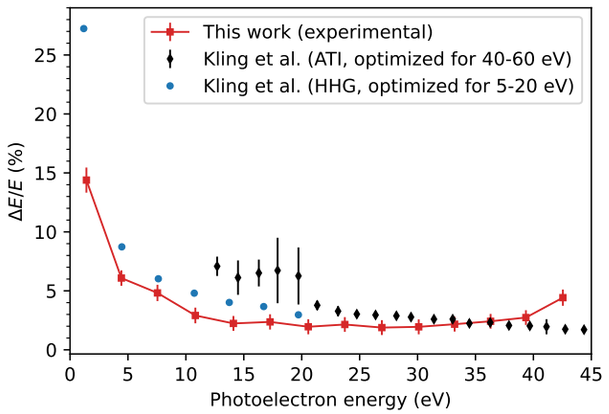

FIG. 7. Comparison of the relative energy resolution of the designed VMI (red square) with that of a thick-lens design[59]. The optimized spectral range and electron signal used to estimate the resolution are given in the legend (black diamond and blue circle).

interaction length, which represents an improvement by a factor of five with respect to the original layout. This is both due to the larger electrostatic lens dimensions and to the optimized electrode shapes. Experimentally, we used a calibrated HHG source to measure the resolution in the 0-44 eV region. A relatively constant value of 2% is obtained in the 15-35 eV range. The difference with the simulations was explained, at low energy, by a larger interaction region than initially simulated and, at high energy, by the resolution of the imaging camera that becomes the limiting factor above 15 eV. This VMIS has been successfully applied to perform attosecond photoionization spectroscopy, namely, the study of the resonant two-photon XUV+IR photoionization of helium through the intermediate $1s3p$ and $1s4p$ states[30]. The high spectral resolution and angular sensitivity have allowed the 3D reconstruction of the attosecond movie of this photoemission event.

Various lines of improvement can be identified for this VMIS. First, an expansion chamber for the gas injection would allow strongly reducing the residual gas pressure, confining the interaction region to that defined by the skimmer. The electrostatic lens resolution would then be significantly increased (for a given value of extractor/repeller voltage), in particular at low photoelectron energy. Second, the imaging of the phosphor screen on the camera should be improved to minimize all sources of aberrations. This would allow an important gain in resolution at high energy. Finally, a flight tube extension is currently being developed and should allow increasing the mass resolution for future applications in ion imaging.

ACKNOWLEDGEMENTS

This research was supported by: Agence Nationale de la Recherche, grant nos. ANR-20-CE30-0007-02-DECAP, ANR-21-CE29-0005-AttoChemistry, and France 2030 ANR-22-EXLU-0002-LUMA; COST, grant no. CA18222-AttoChem; Laserlab-Europe, grant no. EU-H2020-871124; EC, grant no. HORIZON-MSCA-2021-PF-01-101064078-TD-PICO-MF. HJBM acknowledges support by the ERC starting grant SATTOC (101078595).

AUTHOR INFORMATION

Conflict of Interest Statement

The authors have no conflict to disclose.

Contributions

Domique Platzer: Conceptualization (equal); Investigation (lead); Formal analysis (lead) ; Writing – original draft (lead). Alice Autuori: Investigation (equal); Formal analysis (lead); writing - original draft (supporting). Constant Schouder: Formal analysis (supporting); Writing - original draft (equal); Writing - review and editing (lead). Marius Lejman: Investigation (equal); Writing - review and editing (supporting). Lucie Maeder: Formal analysis (supporting); Writing - review and editing (supporting). Hugo Marroux: Writing - review and editing (supporting). Christophe Pothier: Resources (supporting). Pascal Salières: Conceptualization (lead); Formal analysis (supporting); Writing - review and editing (lead). Lionel Poisson: Conceptualization (supporting) ; Writing - review and editing (supporting).

Data Availability Statement

The data that support the findings of this study are available from the corresponding author upon reasonable request.

Appendix A: Energy mapping of the VMI

The mapping between radius and energy is shown in Figure 8 for the expected harmonic peak energy positions. We fit the experimental points by considering either the standard approach with a dependence of the form $E \propto \alpha r^2$ or by adding an additional dependence in r^3. We observe that the latter gives a better agreement to correctly map the peak energy positions over most radius values with a slight mismatch for the zero kinetic energy. This mismatch can also be compensated by adding a r term in the fitting. In all the manuscript, we keep the second expression (green curve) to express the energy axis.

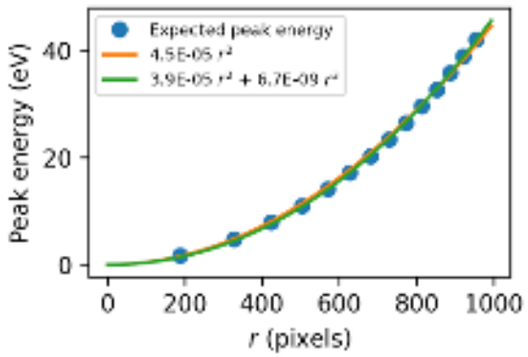

FIG. 8. Mapping between radius and energy extracted from the expected peak energy values (blue circles). Orange and green curves show the best fits considering either a pure r^2 dependence or including a r^3 term.

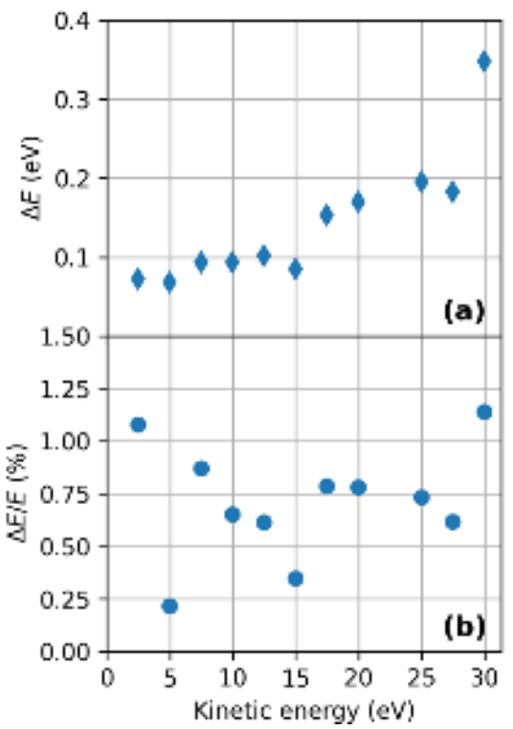

FIG. 9. (a) Xenon Auger Peak 9 width (standard deviation) as a function of the electron final kinetic energy. (b) MBES relative resolution over the 0-30 eV energy range deduced from the peak broadening.

Appendix B: Characterization of the MBES for the HHG source calibration

The reference MBES spectrometer was characterized using secondary electrons associated to the xenon Auger $N_{4,5}OO$ line. The interest of using Auger lines is that their spectral width is intrinsic to the ionized target and thus independent from the ionizing source. This procedure could not be achieved directly in the VMIS as the Auger signal was too weak in this case. High harmonics are generated in a neon gas cell and filtered using a 200-nm zirconium foil that transmits only the XUV radiation above 60 eV. The latter is used to ionize Xenon atoms in their 4d shell leading to inner-shell vacancies that are filled through Auger decay, resulting in secondary electron lines with well-defined energies and spectral widths. In particular, the width (standard deviation) of the $N_{4,5}OO$ singlet line at 29.967 eV energy (noted peak 9 in[72]) was measured to be 67 meV. In their experiment, the absolute resolution was 16 meV which corresponds to an absolute width of 65 meV for peak 9. By using a retarding potential applied between the interaction zone and the time-of-flight tube, we can follow the evolution of the measured peak width for different kinetic energies and thus extract the MBES response function. The results are displayed in Figure 9. From these measurements, we evaluate the effective resolution over the 0-30 eV energy range to be $\approx 0.7\%$ and extrapolate this value to 40 eV to cover the full range.

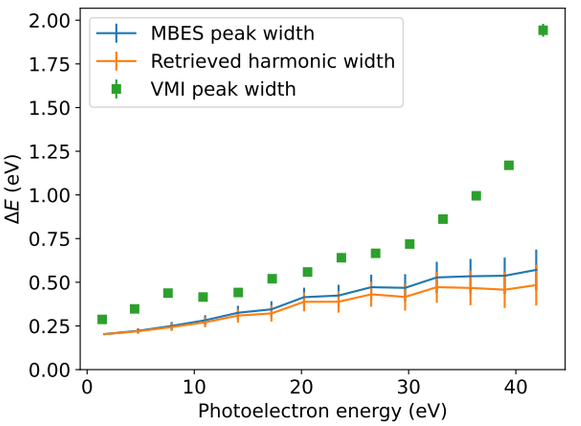

FIG. 10. Photoelectron peak width (standard deviation) measured in the VMIS (green) compared to the width measured in the MBES (blue) and to the harmonic effective width determined using the MBES resolution (orange).

Appendix C: Comparison of harmonic peak widths

The comparison of the harmonic peak widths measured in the MBES and the VMIS is shown in Figure 10 : the MBES spectral resolution is better than the VMIS hence a smaller peak broadening. The settings for the VMIS are the same as in Section IV, respectively -4.889 and -3.885 kV for the repeller and the extractor.

Appendix D: Image circularization

Central symmetry defects in photoelectron images can lead to an artificial broadening of the peaks extracted with Abel

inversion. It additionally translates into a wrong estimation of the anisotropy coefficients. In practice, this sensitivity is the highest for the largest radius (highest kinetic energy electrons). These defects may originate from some imperfections in the magnetic shielding or from a slight asymmetry in the electrodes shape/installation. In our case, we observe a slight angular dependency along the detector radius; electrons with a similar kinetic energy will hit a slightly different detector radius according to their emission direction. For this reason, we apply a circularization procedure on the raw image before applying the Abel inversion transformation. The circularization is based on the mapping of the radius R of the detector onto a corrected radius to include an angular dependency. The formula used is:

$$R_{\mathrm{circ}}(\theta) = R(1 + \alpha \cos\theta) \tag{D1}$$

with α a constant term on the order of 1% and θ the polar angle with respect to the laser polarization axis.

Appendix E: Camera resolution

In contrast to delay-line detectors, imaging of a phosphor screen relies on a camera lens objective that may lead to aberrations and uneven radial resolution along the phosphor screen. To estimate the resolution of the imaging apparatus, we looked at isolated photoelectron signal obtained by ionizing krypton with the harmonic beam generated in Ne and filtered by a 200 nm Zr foil transmitting only the harmonic orders above 60 eV. In that case, we tuned the signal to be sufficiently low such that each island can be considered as originating from an isolated event. By characterizing the mean size of the islands as a function of the radius, we are able to extract the spectral resolution of the camera as a function of energy.

REFERENCES

[1] A. T. J. B. Eppink and D. H. Parker, Review of Scientific Instruments **68**, 3477–3484 (1997).
[2] L. Eisenbud, *The formal properties of nuclear collisions*, PhD Thesis, Princeton University (1948).
[3] E. P. Wigner, "Lower limit for the energy derivative of the scattering phase shift," Phys. Rev. **98**, 145–147 (1955).
[4] F. Smith, "Lifetime matrix in collision theory," Phys. Rev. (1960), 10.1103/PhysRev.118.349.
[5] M. Schultze, M. Fieß, N. Karpowicz, J. Gagnon, M. Korbman, M. Hofstetter, S. Neppl, A. L. Cavalieri, Y. Komninos, T. Mercouris, C. A. Nicolaides, R. Pazourek, S. Nagele, J. Feist, J. Burgdörfer, A. M. Azzeer, R. Ernstorfer, R. Kienberger, U. Kleineberg, E. Goulielmakis, F. Krausz, and V. S. Yakovlev, "Delay in photoemission," Science **328**, 1658–1662 (2010), https://science.sciencemag.org/content/328/5986/1658.full.pdf.
[6] K. Klünder, J. M. Dahlström, M. Gisselbrecht, T. Fordell, M. Swoboda, D. Guénot, P. Johnsson, J. Caillat, J. Mauritsson, A. Maquet, R. Taïeb, and A. L'Huillier, "Probing single-photon ionization on the attosecond time scale," Phys. Rev. Lett. **106**, 143002 (2011).
[7] S. Haessler, B. Fabre, J. Higuet, J. Caillat, T. Ruchon, P. Breger, B. Carré, E. Constant, A. Maquet, E. Mével, P. Salières, R. Taïeb, and Y. Mairesse, "Phase-resolved attosecond near-threshold photoionization of molecular nitrogen," Phys. Rev. A **80**, 011404 (2009).
[8] M. Huppert, I. Jordan, D. Baykusheva, A. von Conta, and H. J. Wörner, "Attosecond delays in molecular photoionization," Phys. Rev. Lett. **117**, 093001 (2016).
[9] L. Seiffert, Q. Liu, S. Zherebtsov, A. Trabattoni, P. Rupp, M. C. Castrovilli, M. Galli, F. Süßmann, K. Wintersperger, J. Stierle, G. Sansone, L. Poletto, F. Frassetto, I. Halfpap, V. Mondes, C. Graf, E. Rühl, F. Krausz, M. Nisoli, T. Fennel, F. Calegari, and M. Kling, "Attosecond chronoscopy of electron scattering in dielectric nanoparticles," Nature Physics **13**, 766–770 (2017).
[10] I. Jordan, M. Huppert, D. Rattenbacher, M. Peper, D. Jelovina, C. Perry, A. von Conta, A. Schild, and H. J. Wörner, "Attosecond spectroscopy of liquid water," Science **369**, 974–979 (2020), https://www.science.org/doi/pdf/10.1126/science.abb0979.
[11] A. L. Cavalieri, N. Müller, T. Uphues, V. S. Yakovlev, A. Baltuška, B. Horvath, B. Schmidt, L. Blümel, R. Holzwarth, S. Hendel, *et al.*, "Attosecond spectroscopy in condensed matter," Nature **449**, 1029 (2007).
[12] P. M. Paul, E. S. Toma, P. Breger, G. Mullot, F. Augé, P. Balcou, H. G. Muller, and P. Agostini, "Observation of a train of attosecond pulses from high harmonic generation," Science **292**, 1689–1692 (2001), https://www.science.org/doi/pdf/10.1126/science.1059413.
[13] J. Itatani, F. Quéré, G. L. Yudin, M. Y. Ivanov, F. Krausz, and P. B. Corkum, "Attosecond streak camera," Phys. Rev. Lett. **88**, 173903 (2002).
[14] R. Kienberger, E. Goulielmakis, M. Uiberacker, A. Baltuska, V. Yakovlev, F. Bammer, A. Scrinzi, T. Westerwalbesloh, U. Kleineberg, U. Heinzmann, M. Drescher, and F. Krausz, "Atomic transient recorder," Nature **427**, 817–821 (2004).
[15] M. Kotur, D. Guénot, Jiménez-Galán, D. Kroon, E. W. Larsen, M. Louisy, S. Bengtsson, M. Miranda, J. Mauritsson, C. L. Arnold, S. E. Canton, M. Gisselbrecht, T. Carette, J. M. Dahlström, E. Lindroth, A. Maquet, L. Argenti, F. Martín, and A. L'Huillier, "Spectral phase measurement of a Fano resonance using tunable attosecond pulses," Nature Communications **7**, 10566 (2016).
[16] V. Gruson, L. Barreau, Á. Jiménez-Galan, F. Risoud, J. Caillat, A. Maquet, B. Carré, F. Lepetit, J.-F. Hergott, T. Ruchon, L. Argenti, R. Taïeb, F. Martín, and P. Salières, "Attosecond dynamics through a Fano resonance: Monitoring the birth of a photoelectron," Science **354**, 734–738 (2016), https://science.sciencemag.org/content/354/6313/734.full.pdf.
[17] D. Busto, L. Barreau, M. Isinger, M. Turconi, C. Alexandridi, A. Harth, S. Zhong, R. J. Squibb, D. Kroon, S. Plogmaker, M. Miranda, Jiménez-Galán, L. Argenti, C. L. Arnold, R. Feifel, F. Martín, M. Gisselbrecht, A. L'Huillier, and P. Salières, "Time–frequency representation of autoionization dynamics in helium," Journal of Physics B: Atomic, Molecular and Optical Physics **51**, 044002 (2018).
[18] M. Turconi, L. Barreau, D. Busto, M. Isinger, C. Alexandridi, A. Harth, R. J. Squibb, D. Kroon, C. L. Arnold, R. Feifel, M. Gisselbrecht, L. Argenti, F. Martín, A. L. 'Huillier, and P. Salières, "Spin–orbit-resolved spectral phase measurements around a fano resonance," Journal of Physics B: Atomic, Molecular and Optical Physics **53**, 184003 (2020).
[19] C. Alexandridi, D. Platzer, L. Barreau, D. Busto, S. Zhong, M. Turconi, L. Neoričić, H. Laurell, C. L. Arnold, A. Borot, J.-F. Hergott, O. Tcherbakoff, M. Lejman, M. Gisselbrecht, E. Lindroth, A. L'Huillier, J. M. Dahlström, and P. Salières, "Attosecond photoionization dynamics in the vicinity of the cooper minima in argon," Phys. Rev. Res. **3**, L012012 (2021).
[20] S. A. Aseyev, Y. Ni, L. J. Frasinski, H. G. Muller, and M. J. J. Vrakking, "Attosecond angle-resolved photoelectron spectroscopy," Phys. Rev. Lett. **91**, 223902 (2003).
[21] K. Varjú, P. Johnsson, J. Mauritsson, T. Remetter, T. Ruchon, Y. Ni, F. Lépine, M. Kling, J. Khan, K. J. Schafer, M. J. J. Vrakking, and A. L'Huillier, "Angularly resolved electron wave packet interferences*," Journal of Physics B: Atomic, Molecular and Optical Physics **39**, 3983 (2006).
[22] J. M. Dahlström and E. Lindroth, "Corrigendum: Study of attosecond delays using perturbation diagrams and exterior complex scaling (dahlström and lindroth 2014j. phys. b: At. mol. opt. phys.47124012)," Journal of Physics B: Atomic, Molecular and Optical Physics **49**, 209501 (2016).
[23] S. Banerjee, P. C. Deshmukh, V. K. Dolmatov, S. T. Manson, and A. S. Kheifets, "Strong dependence of photoionization time delay on energy and angle in the neighborhood of fano resonances," Phys. Rev. A **99**, 013416 (2019).

[24]A. S. Kheifets, D. Toffoli, and P. Decleva, "Angular dependent time delay near correlation induced cooper minima," Journal of Physics B: Atomic, Molecular and Optical Physics (2020).

[25]S. Heuser, A. Jiménez Galán, C. Cirelli, C. Marante, M. Sabbar, R. Boge, M. Lucchini, L. Gallmann, I. Ivanov, A. S. Kheifets, J. M. Dahlström, E. Lindroth, L. Argenti, F. Martín, and U. Keller, "Angular dependence of photoemission time delay in helium," Phys. Rev. A **94**, 063409 (2016).

[26]C. Cirelli, C. Marante, S. Heuser, C. L. M. Petersson, Á. Jiménez-Galán, L. Argenti, S. Zhong, D. Busto, M. Isinger, S. Nandi, S. Maclot, L. Rading, P. Johnsson, M. Gisselbrecht, M. Lucchini, L. Gallmann, J. M. Dahlström, E. Lindroth, A. L'Huillier, F. Martín, and U. Keller, "Anisotropic photoemission time delays close to a fano resonance," Nature Communications **9**, 955 (2018).

[27]D. M. Villeneuve, P. Hockett, M. J. J. Vrakking, and H. Niikura, "Coherent imaging of an attosecond electron wave packet," Science **356**, 1150–1153 (2017), https://www.science.org/doi/pdf/10.1126/science.aam8393.

[28]S. Beaulieu, A. Comby, A. Clergerie, J. Caillat, D. Descamps, N. Dudovich, B. Fabre, R. Géneaux, F. Légaré, S. Petit, B. Pons, G. Porat, T. Ruchon, R. Taïeb, V. Blanchet, and Y. Mairesse, "Attosecond-resolved photoionization of chiral molecules," Science **358**, 1288–1294 (2017), https://www.science.org/doi/pdf/10.1126/science.aao5624.

[29]D. Busto, J. Vinbladh, S. Zhong, M. Isinger, S. Nandi, S. Maclot, P. Johnsson, M. Gisselbrecht, A. L'Huillier, E. Lindroth, and J. M. Dahlström, "Fano's propensity rule in angle-resolved attosecond pump-probe photoionization," Phys. Rev. Lett. **123**, 133201 (2019).

[30]A. Autuori, D. Platzer, M. Lejman, G. Gallician, L. Maëder, A. Covolo, L. Bosse, M. Dalui, D. Bresteau, J.-F. Hergott, O. Tcherbakoff, H. J. B. Marroux, V. Loriot, F. Lépine, L. Poisson, R. Taïeb, J. Caillat, and P. Salières, "Anisotropic dynamics of two-photon ionization: An attosecond movie of photoemission," Science Advances **8**, eabl7594 (2022), https://www.science.org/doi/pdf/10.1126/sciadv.abl7594.

[31]J. Vos, L. Cattaneo, S. Patchkovskii, T. Zimmermann, C. Cirelli, M. Lucchini, A. Kheifets, A. S. Landsman, and U. Keller, "Orientation-dependent stereo wigner time delay and electron localization in a small molecule," Science **360**, 1326–1330 (2018), https://www.science.org/doi/pdf/10.1126/science.aao4731.

[32]L. Cattaneo, J. Vos, R. Y. Bello, A. Palacios, S. Heuser, L. Pedrelli, M. Lucchini, C. Cirelli, F. Martín, and U. Keller, "Attosecond coupled electron and nuclear dynamics in dissociative ionization of h2," Nature Physics (2018).

[33]V. Loriot, A. Marciniak, G. Karras, B. Schindler, G. Renois-Predelus, I. Compagnon, B. Concina, R. Brédy, G. Celep, C. Bordas, E. Constant, and F. Lépine, "Angularly resolved RABBITT using a second harmonic pulse," Journal of Optics **19**, 114003 (2017).

[34]J. Fuchs, N. Douguet, S. Donsa, F. Martín, J. Burgdörfer, L. Argenti, L. Cattaneo, and U. Keller, "Time delays from one-photon transitions in the continuum," Optica **7**, 154–161 (2020).

[35]J. Joseph, F. Holzmeier, D. Bresteau, C. Spezzani, T. Ruchon, J. F. Hergott, O. Tcherbakoff, P. D'Oliveira, J. C. Houver, and D. Dowek, "Angle-resolved studies of xuv–ir two-photon ionization in the rabbitt scheme," Journal of Physics B: Atomic, Molecular and Optical Physics **53**, 184007 (2020).

[36]Busto, David, Laurell, Hugo, Finkelstein-Shapiro, Daniel, Alexandridi, Christiana, Isinger, Marcus, Nandi, Saikat, Squibb, Richard J., Turconi, Margherita, Zhong, Shiyang, Arnold, Cord L., Feifel, Raimund, Gisselbrecht, Mathieu, Salières, Pascal, Pullerits, Tönu, Martín, Fernando, Argenti, Luca, and L'Huillier, Anne, "Probing electronic decoherence with high-resolution attosecond photoelectron interferometry," Eur. Phys. J. D **76**, 112 (2022).

[37]J. Ullrich, R. Moshammer, R. Dörner, O. Jagutzki, V. Mergel, H. Schmidt-Böcking, and L. Spielberger, "Recoil-ion momentum spectroscopy," Journal of Physics B: Atomic, Molecular and Optical Physics **30**, 2917–2974 (1997).

[38]R. Dörner, V. Mergel, O. Jagutzki, L. Spielberger, J. Ullrich, R. Moshammer, and H. Schmidt-Böcking, "Cold target recoil ion momentum spectroscopy: a 'momentum microscope' to view atomic collision dynamics," Physics Reports **330**, 95 – 192 (2000).

[39]N. A. Cherepkov, G. Raseev, J. Adachi, Y. Hikosaka, K. Ito, S. Motoki, M. Sano, K. Soejima, and A. Yagishita, "K-shell photoionization of co: Ii. determination of dipole matrix elements and phase differences," Journal of Physics B: Atomic, Molecular and Optical Physics **33**, 4213 (2000).

[40]M. Lebech, J. C. Houver, A. Lafosse, D. Dowek, C. Alcaraz, L. Nahon, and R. R. Lucchese, "Complete description of linear molecule photoionization achieved by vector correlations using the light of a single circular polarization," The Journal of Chemical Physics **118**, 9653–9663 (2003), _eprint: https://pubs.aip.org/aip/jcp/article-pdf/118/21/9653/19024765/9653_1_online.pdf.

[41]D. Rolles, Z. Pešić, M. Perri, R. Bilodeau, G. Ackerman, B. Rude, A. Kilcoyne, J. Bozek, and N. Berrah, Nuclear Instruments and Methods in Physics Research Section B: Beam Interactions with Materials and Atoms **261**, 170 – 174 (2007), the Application of Accelerators in Research and Industry.

[42]L. Rading, J. Lahl, S. Maclot, F. Campi, H. Coudert-Alteirac, B. Oostenrijk, J. Peschel, H. Wikmark, P. Rudawski, M. Gisselbrecht, and P. Johnsson, "A versatile velocity map ion-electron covariance imaging spectrometer for high-intensity xuv experiments," Applied Sciences **8** (2018), 10.3390/app8060998.

[43]G. Basnayake, Y. Ranathunga, S. K. Lee, and W. Li, "Three-dimensional (3d) velocity map imaging: from technique to application," Journal of Physics B: Atomic, Molecular and Optical Physics **55**, 023001 (2022).

[44]D. Townsend, M. P. Minitti, and A. G. Suits, "Direct current slice imaging," Review of Scientific Instruments **74**, 2530–2539 (2003), https://doi.org/10.1063/1.1544053.

[45]M. Wollenhaupt, M. Krug, J. Köhler, T. Bayer, C. Sarpe-Tudoran, and T. Baumert, "Three-dimensional tomographic reconstruction of ultrashort free electron wave packets," Applied Physics B **95**, 647–651 (2009).

[46]A. T. Clark, J. P. Crooks, I. Sedgwick, R. Turchetta, J. W. L. Lee, J. J. John, E. S. Wilman, L. Hill, E. Halford, C. S. Slater, B. Winter, W. H. Yuen, S. H. Gardiner, M. L. Lipciuc, M. Brouard, A. Nomerotski, and C. Vallance, "Multimass velocity-map imaging with the pixel imaging mass spectrometry (pimms) sensor: An ultra-fast event-triggered camera for particle imaging," The Journal of Physical Chemistry A **116**, 10897–10903 (2012), pMID: 23102270, https://doi.org/10.1021/jp309860t.

[47]A. Zhao, M. van Beuzekom, B. Bouwens, D. Byelov, I. Chakaberia, C. Cheng, E. Maddox, A. Nomerotski, P. Svihra, J. Visser, V. Vrba, and T. Weinacht, "Coincidence velocity map imaging using tpx3cam, a time stamping optical camera with 1.5 ns timing resolution," Review of Scientific Instruments **88**, 113104 (2017), https://doi.org/10.1063/1.4996888.

[48]D. A. Debrah, G. A. Stewart, G. Basnayake, A. Nomerotski, P. Svihra, S. K. Lee, and W. Li, "Developing a camera-based 3D momentum imaging system capable of 1 Mhits/s," Review of Scientific Instruments **91**, 023316 (2020), https://pubs.aip.org/aip/rsi/article-pdf/doi/10.1063/1.5138731/15660427/023316_1_online.pdf.

[49]E. S. Goudreau, A. E. Boguslavskiy, D. J. Moffatt, V. Makhija, M. Hemsworth, R. Lausten, C. Marceau, I. Wilkinson, and A. Stolow, "Time-stretched multi-hit 3D velocity map imaging of photoelectrons," Review of Scientific Instruments **94**, 063002 (2023), https://pubs.aip.org/aip/rsi/article-pdf/doi/10.1063/5.0149897/17996966/063002_1_5.0149897.pdf.

[50]C. Cheng, G. Moğol, T. Weinacht, A. Nomerotski, and C. Trallero-Herrero, "3D velocity map imaging of electrons with TPX3CAM," Review of Scientific Instruments **93**, 013003 (2022), https://pubs.aip.org/aip/rsi/article-pdf/doi/10.1063/5.0071804/16575457/013003_1_online.pdf.

[51]M. Davino, E. McManus, N. G. Helming, C. Cheng, G. Moğol, Z. Rodnova, G. Harrison, K. Watson, T. Weinacht, G. N. Gibson, *et al.*, "A plano–convex thick-lens velocity map imaging apparatus for direct, high resolution 3d momentum measurements of photoelectrons with ion time-of-flight coincidence," Review of Scientific Instruments **94** (2023).

[52]E. W. Hansen and P.-L. Law, "Recursive methods for computing the abel transform and its inverse," J. Opt. Soc. Am. A **2**, 510–520 (1985).

[53]G. A. Garcia, L. Nahon, and I. Powis, "Two-dimensional charged particle image inversion using a polar basis function expansion," Review of Scientific Instruments **75**, 4989–4996 (2004), https://pubs.aip.org/aip/rsi/article-pdf/75/11/4989/19144214/4989_1_online.pdf.

[54]L. Montgomery Smith, D. R. Keefer, and S. Sudharsanan, "Abel inversion using transform techniques," Journal of Quantitative Spectroscopy and Radiative Transfer **39**, 367–373 (1988).

[55]C. J. Dasch, "One-dimensional tomography: a comparison of abel, onion-peeling, and filtered backprojection methods," Appl. Opt. **31**, 1146–1152 (1992).

[56]S. Li, E. G. Champenois, R. Coffee, Z. Guo, K. Hegazy, A. Kamalov, A. Natan, J. O'Neal, T. Osipov, M. Owens, D. Ray, D. Rich, P. Walter, A. Marinelli, and J. P. Cryan, "A co-axial velocity map imaging spectrometer for electrons," AIP Advances **8**, 115308 (2018), https://doi.org/10.1063/1.5046192.

[57]K. Mizuse, R. Fujimoto, and Y. Ohshima, "Space-slice ion imaging: High slice resolution imaging in the polarization plane of arbitrarily polarized ionizing light," Review of Scientific Instruments **90**, 103107 (2019), https://doi.org/10.1063/1.5110690.

[58]G. A. Garcia, L. Nahon, C. J. Harding, E. A. Mikajlo, and I. Powis, Review of Scientific Instruments **76**, 053302 (2005).

[59]N. G. Kling, D. Paul, A. Gura, G. Laurent, S. De, H. Li, Z. Wang, B. Ahn, C. H. Kim, T. K. Kim, I. V. Litvinyuk, C. L. Cocke, I. Ben-Itzhak, D. Kim, and M. F. Kling, Journal of Instrumentation **9**, P05005 (2014).

[60]L. Dakroub, T. Sinyakova, D. Cubaynes, C. Bomme, L. Chopineau, G. Garcia, O. Peyrusse, F. Quéré, C. Bourassin-Bouchet, and A. Klisnick, "Laser-dressed photoionization for the temporal characterization of attosecond pulses generated from plasma mirrors," The European Physical Journal Special Topics **232**, 2055–2067 (2023).

[61]H. L. Offerhaus, C. Nicole, F. Lépine, C. Bordas, F. Rosca-Pruna, and M. J. J. Vrakking, "A magnifying lens for velocity map imaging of electrons and ions," Review of Scientific Instruments **72**, 3245–3248 (2001), https://doi.org/10.1063/1.1386909.

[62]S. Skruszewicz, J. Passig, A. Przystawik, N. Truong, M. Köther, J. Tiggesbäumker, and K.-H. Meiwes-Broer, "A new design for imaging of fast energetic electrons," International Journal of Mass Spectrometry **365-366**, 338 – 342 (2014), special issue: Tilmann Märk.

[63]E. Wrede, S. Laubach, S. Schulenburg, A. Brown, E. R. Wouters, A. J. Orr-Ewing, and M. N. R. Ashfold, The Journal of Chemical Physics **114**, 2629–2646 (2001).

[64]B. Marchetti, T. N. V. Karsili, O. Kelly, P. Kapetanopoulos, and M. N. R. Ashfold, The Journal of Chemical Physics **142**, 224303 (2015).

[65]D. A. Dahl, "simion for the personal computer in reflection," International Journal of Mass Spectrometry **200**, 3–25 (2000), volume 200: The state of the field as we move into a new millenium.

[66]Values given by the constructor.

[67]K. Codling, R. G. Houlgate, J. B. West, and P. R. Woodruff, "Angular distribution and photoionization measurements on the 2p and 2s electrons in neon," Journal of Physics B: Atomic and Molecular Physics **9**, L83 (1976).

[68]S. J. Weber, B. Manschwetus, M. Billon, M. Böttcher, M. Bougeard, P. Breger, M. Géléoc, V. Gruson, A. Huetz, N. Lin, Y. J. Picard, T. Ruchon, P. Salières, and B. Carré, "Flexible attosecond beamline for high harmonic spectroscopy and XUV/near-IR pump probe experiments requiring long acquisition times," Review of Scientific Instruments **86**, 033108 (2015), _eprint: https://pubs.aip.org/aip/rsi/article-pdf/doi/10.1063/1.4914464/15818739/033108_1_online.pdf.

[69]Bresteau, D., Spezzani, C., Tcherbakoff, O., Hergott, J.-F., Lepetit, F., D'Oliveira, P., Salières, P., Géneaux, R., Luttmann, M., Vadillo-Torre, I., Lenfant, J., Weber, S. J., Dehlinger, M., Meltchakov, E., Delmotte, F., Bourassin-Bouchet, C., Im, J., Chen, Z., Caillaux, J., Zhang, J., Marsi, M., Barreau, L., Poisson, L., Dowek, D., Fanciulli, M., Heckmann, O., Richter, M. C., Hricovini, K., Sebdaoui, M., Dennetiere, D., Polack, F., and Ruchon, T., "Fab10: a user-oriented bandwidth-tunable extreme ultraviolet lightsource for investigations of femtosecond to attosecond dynamics in gas and condensed phases," Eur. Phys. J. Spec. Top. **232**, 2011–2029 (2023).

[70]G. R. Harrison, J. C. Vaughan, B. Hidle, and G. M. Laurent, "Davis: A direct algorithm for velocity-map imaging system," The Journal of Chemical Physics **148**, 194101 (2018), https://doi.org/10.1063/1.5025057.

[71]A. Maquet and R. TaÏeb, "Two-colour ir+xuv spectroscopies: the "soft-photon approximation"," Journal of Modern Optics **54**, 1847–1857 (2007), https://doi.org/10.1080/09500340701306751.

[72]T. Carroll, J. Bozek, E. Kukk, V. Myrseth, L. Sæthre, T. Thomas, and K. Wiesner, "Xenon n4,5oo auger spectrum—a useful calibration source," Journal of Electron Spectroscopy and Related Phenomena **125**, 127–132 (2002).